Electron-Beam Welding of Laser Powder-Bed-Fused Inconel 718

Akash Sali, Vivek Patel, James Hyder, David Hyder, Mike Corliss and Wayne Hung

ABSTRACT

This study explores the application of Electron-Beam Welding (EBW) for joining Laser Powder-Bed-Fused Inconel 718 (L-PBF IN718) superalloy. Three different levels of electron beam speed and beam current were explored to give nine different electron beam heat inputs for experimentation. To define the weld characteristics microhardness, tensile, and fractography analysis using scanning electron microscopy, optical microscopy, and energy dispersive spectroscopy were conducted. Typical nail-shaped weld geometry was observed with penetration depth proportional to heat input. Most welded samples exceeded the yield strength (600MPa) and tensile strength (920MPa) requirements from the ASTM F3055 specifications for additively manufactured IN718, however, the specimens did not meet the ductility requirements (27%). Brittleness of the weld was attributed to the presence of brittle secondary phases in the weld matrix, and unfused metal powder of adjacent L-PBF layers. Post-processing heat treatments were recommended to improve the weld quality while improving the ductility of EBW joints.

Keywords: Electron Beam Welding; Inconel 718; Laser Powder Bed Fusion; Microhardness; Mechanical Properties; Fractography.

1 INTRODUCTION

Additive manufacturing has exceeded from being a mere prototyping method to a method of production given its advantage in generating near-net-shaped parts with complex geometries. Selective Laser Melting (SLM) or Laser Powder-Bed-Fusion (L-PBF) process is additive manufacturing (AM) technique in which adjacent layers of fine metal powder are selectively fused with a powerful laser beam. Due to this layer-wise method of producing metal components and quality products, L-PBF has gained popularity in the aerospace, defence, energy, medical, and automotive industry. However, due to the limited size of current powdered fusion machines and high costs associated with the production of large parts, L-PBF is not being utilized to its full potential currently and imposes restrictions on the size of the parts that can be printed using this method. Thus, there is a need to explore an efficient way to join these parts reliably.

Nomenclature:

AM	Additive Manufacturing
DTA	Differential Thermal Analysis
EBW	Electron Beam Welding
EDM	Electrical Discharge Machining
DTA	Differential Thermal Analysis
ε_f	Elongation
HAZ	Heat Affected Zone
IN718	Inconel 718
L-PBF	Laser Powder Bed Fusion
SEM	Scanning Electron Microscopy
SLM	Selective Laser Melting
TIG	Tungsten Inert Gas Welding
UTS	Ultimate Tensile Strength
YS	Yield Strength

Akash Sali[1], Vivek Patel[1], Wayne Hung[1] ✉, James Hyder[2], David Hyder[2], Mike Corliss[2]

[1]Texas A&M University,
College Station, Texas 77843, USA
[2]Knust-Godwin LLC,
Katy, Texas 77494, USA
E-mail: hung@tamu.edu

Inconel 718 (IN718) is a nickel-based superalloy that has an excellent performance in terms of tensile strength, hardness, and corrosion resistance at high temperatures up to 600˚C [1]. Due to this advantage, IN718 is widely used for high-temperature applications in the energy, defence, and aerospace industries. The strain hardening property of IN718 imposes restrictions on the complexity and cost of conventional machining processes [2]. Thus, L-PBF has gained popularity as a preferred method of producing complex-shaped IN718 parts.

Although expensive and need complex control systems, Electron Beam Welding (EBW) has proven to be an excellent welding method that produces welds with deep penetrations, minimal heat-affected zones, and high joint strength [3]. This method also imposes minimal thermal impact and prevents excessive deterioration of microstructural and metallurgical properties of a weldment. Due to limited published literature on EBW of additive manufactured metals, this research explores the possibility of using EBW to join L-PBF IN718 parts, examines the resulted weld quality, and compares mechanical properties of welded specimens against the standard ASTM material specifications for AM IN718.

2 LITERATURE REVIEW

Microstructures and mechanical properties of L-PBF IN718 have been studied; however, a comprehensive study on EBW of L-PBF IN718 is yet to be found. Background studies of EBW of rolled IN718 and aluminium alloys were found together with brazing and arc welding of L-PBF IN718.

2.1 Microstructure of IN718

The IN718 is a nickel-based superalloy (Ni 50-55%, Cr 17-21%, Fe 17%, Nb 4.75-5.5%, Mo 2.8-3.3%, Ti 0.65-1.15%, Al 0.2-0.8%, C<0.8%, Co<1.0%, Cu<0.3%, Si<0.35%, Mg<0.35% [4]). This alloy exhibits high tensile strength and depicts high creep resistance at higher temperatures owing to the formation and stability of various secondary phases in its microstructure [5]. These phases also cause strain hardening and affect the ductility of the IN718. A solidification phase diagram of IN718 was prepared using phases formed after a non-equilibrium welding process in a research study [6]. The specimens were heat-treated at 1000˚C for 1hr. Differential Thermal Analysis (DTA) was performed to define the solidification phases. Heating was conducted in an argon-controlled environment at 10˚C/min up to 1450˚C. The samples were cooled through all significant solidification temperatures at a rate of 10˚C/s. The solidification phase diagram based on the composition of Nb at various temperatures is presented in Figure 1.

Molten IN718 undergoes solidification in three stages [7]:

— First, the liquid solidifies to secondary γ phases (γ' and γ'') and led to the formation of Nb, C, Ti, and Al precipitate in the interdendritic regions.

— Second, the carbon present in the alloy was consumed by the segregated particles leading to the formation of intermetallic carbides.

— Third, further enrichment of the solute led to Laves phase formation. The segregated Nb was shared by all the secondary phases δ (Incoherent - Ni_3Nb), γ' (Ni_3Al), γ'' (Ni_3Nb), Laves (($Ni,Cr,Fe)_2(Nb,Mo,Ti)$), and Carbides during solidification.

Thus, a higher percentage of one of the phases meant less percentage of the other. Of these phases, the γ' and γ'' are the strengthening phases and should be present in the higher percentage. Thus, it is necessary to control the formation of the other deteriorating phases like the δ, Laves, and carbides. These phases are formed due to fast cooling as found for welding or laser processing. During the L-PBF process, although the metal may reach the specified temperatures since the laser beam moves at a relatively fast feed rate, the exact phases that will be formed doing the process cannot be predicted accurately. However, the phase diagram for equilibrium conditions with a very slow cooling rate only gives a general idea of different secondary phases of the IN718 alloy.
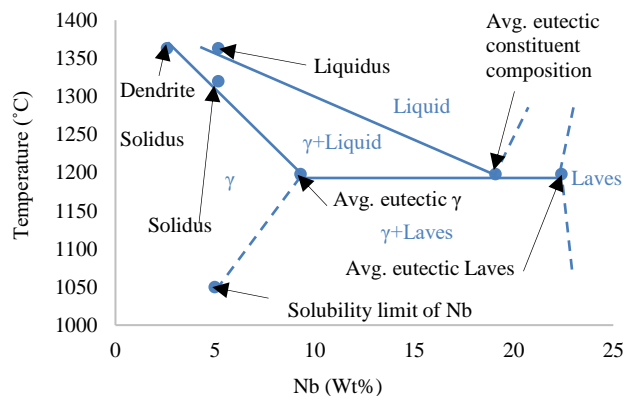

Figure 1: Solidification diagram for IN718 [6]

2.2 Anisotropic Properties of L-PBF IN718

Since L-PBF metals have properties different than the conventionally manufactured counterparts due to the layer-wise building followed by quick solidification, localized heating, and cooling which leads to residual stresses, and development of pores due to lack of fusion or shrinkage [8]. The building of L-PBF components layer-by-layer also tends to produce anisotropic mechanical properties. To establish this theory, mechanical properties of the L-PBF IN718 samples with (a) building direction parallel to the testing direction (Vertical), and (b) building direction perpendicular to the testing direction (Horizontal) were compared. It was found that:

— Building direction did not affect the hardness of both samples.
— The difference in tensile strength and elongation about 100MPa and 3-8% respectively were observed between the horizontal and vertical samples in both as-printed and direct aged samples.

This directional variation was due to different residual stresses, accumulated dislocations, and crystallographic orientation in the loading direction. The claim was also supported by another research [9] which associated the observed difference in mechanical properties with a higher number of inter-layer joints in the loading direction and to the different distribution of the γ" phase.

2.3 EBW of Rolled IN718

Since no previously published literature was found for EBW of L-PBF IN718, various literature on EBW of rolled IN718 was studied to establish the base for this study.

The effect of various pre-weld heat treatment conditions on heat-affected zone formation after EBW was studied using microhardness measurements [10]. The sheets of IN718 samples were solution treated at 950°C for 1hr followed by water quenching. Some were further treated by precipitation treatment at 760 °C for 4hr followed by water quenching. EBW was done with the first pass (50kV, 100mA, 2173mm/min, and 3.46mm focus depth), following with the second pass (50kV, 60mA, 1524mm/min, and 3.42mm focus depth). The hardness test result revealed a lower hardness of the fusion zone/ HAZ as compared to base metal for precipitation pre-treated samples. The as-received and solution pre-treated samples had a uniform hardness distribution. The spike in hardness values for precipitation treated samples was associated with their high thermal sensitivity and precipitation of γ' and γ" phases in the HAZ.

An attempt was made to reduce the formation of Laves phase and niobium segregation on solution-treated IN718 plates to improve the tensile properties of the weld [11]. Electron beam oscillations during the welding process were performed: (i) Un-oscillated welding: 55kV, 22mA, 1.5m/min, and focus above the sample surface; (ii) Elliptical oscillated welding: 15Hz frequency, 55kV, 25mA, 1.5m/min, and focus on the sample surface. The welded samples were treated at two different solutionising conditions: 980 °C/1h air cooling and 1080 °C/1h, air cooling. Some samples were further treated using dual aging at 720 °C/8h, furnace cooling followed by 620 °C/ 8h, air cooling. The elliptical weld oscillations were the most effective in reducing the segregation of niobium and Laves formation and achieving a higher tensile test. Oscillating welds led to the formation of several small weld pools at any point in time leading to better cooling rate, high fluid flow, and reduced thermal gradients in the weld pool leading to better weld quality.

The EBW heat input (equation 1) affects the fusion zone and HAZ microstructure while controlling liquation cracking and segregation of alloying elements [12].

$$Heat\ Input\ \left(\frac{J}{m}\right) = \frac{Beam\ Current\ (A) \times Beamvoltage\ (V)}{Welding\ speed\ \left(\frac{m}{s}\right)} \tag{1}$$
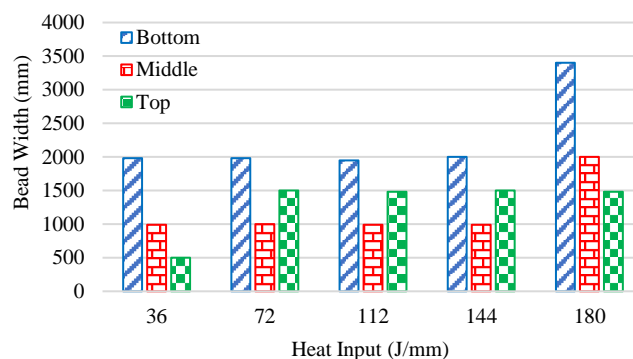

Figure 2: Weld Width versus Heat Input [12]

Cold rolled IN718 sheets were EBW'ed at 30mm/s feed rate, 60kV voltage, and currents of 18mA, 36mA, 56mA, 72mA, and 90mA. Microstructural analysis revealed that the width of the fusion zone increased with increasing heat input. This was due to the higher melting of base metal at a higher beam current. The width of the weld also varied along with the depth of penetration as seen in Fig. 2. But heat input variation did influence the formation of micro-fissures in HAZ. The lowest heat input sample indicated the presence of HAZ micro-fissures while all other samples were free from it. This was associated with a higher temperature gradient in HAZ at lower heat input providing a higher grain boundary area for cracking [12].

Pre-weld heat treatments also affect the geometry of the weld [13]. Plates of IN718 were subjected to various heat treatments: 1100 °C/1 h, air-cooled; 1040 °C/1 h, air-cooled; 950 °C/1 h, air-cooled. EBW parameters were 125kV, 65mA, and speeds of 1270, 1207, and 1143mm/min. Weld with a nail-head shape was observed when the sample was treated at 1000˚C for an hour and cooled by air cooling as opposed to the stemless wine glass shape in as-received condition. The total HAZ crack length also increased from 40μm to 675μm due to the pre-heating of the base metal. The microstructure analysis also revealed an increase in the Laves formation and a decrease in HAZ cracking as the welding speed was decreased.

A variation in mechanical properties of a 12mm thick penetration weld on as-received IN718 hot rolled plates with EBW parameters of 60kV, 120mA, and 11mm/s for the first pass and 60kV, 30mA, and 11mm/s for the second pass was observed after tensile testing at 650˚C [14]. The tensile strength was best at the bottom of the weld (1185MPa) and worst at the top (1100MPa). The strength of the base metal was 1240MPa. Elongation at fracture also increased from the top (9%) to bottom (18%). This was due to the brittle fracture surface of the weld at the top. The elongation of the base metal was 22%.

The EBW was successfully utilized to join as-received 12.7mm-thick rolled IN718 plates [15]. EBW parameters were: 50kV constant voltage, current of 65, 60, and 50mA, and speeds of 660.4, 787.4, and 914.4mm/min. Weld area and penetration depth increased with increasing heat input. However, root keyhole defects were observed at a heat input higher than 247.6J/mm. Samples welded at low heat inputs exhibited higher tensile strength that exceeded base material specification (837MPa) and fractured outside the weld with typical elongation of 57% while those samples that welded at a higher heat input fractured at the welds.

In summary, EBW has been successfully utilized to join wrought IN718 plates. Pre-welding thermal treatment, optimal EBW process parameters, and oscillations of the beam help to achieve a favourable microstructure, therefore, resulting in good mechanical quality. These observations were utilized during the planning of our research.

2.4 Defects Formation in EBW

Porosity is found in the welded zone due to (i) the presence of releasing gas in molten metal, (ii) trapping of void due to the dynamic flow of molten metals at certain viscosity, and (iii) shrinkage cavity from molten metal at fast cooling rate.

Instability of the keyholes in the partial penetration welds, dissolved and trapped gases and solidification shrinkage led to the formation of voids and pores in EBW of rolled CP-titanium alloy [16], [17]. The fast-cooling rates of EBW associated with high welding beam speed and narrow weld area prevented the escape of the gas bubbles, therefore, formed pores in the weld zone. Small pores were also seen on the fusion zone boundary due to the poor flow of molten metal over the gases trapped on the solid walls at the fusion zone boundaries. The irregular-shaped voids were formed due to shrinkage caused by the volumetric difference of liquid and solid phases during solidification. An offset between the weld path and joint location was stipulated to cause the melt bubbles to travel sideways and keep growing preventing them from getting released from the melt pool thus giving rise to the porosity at the top of the weld zone.
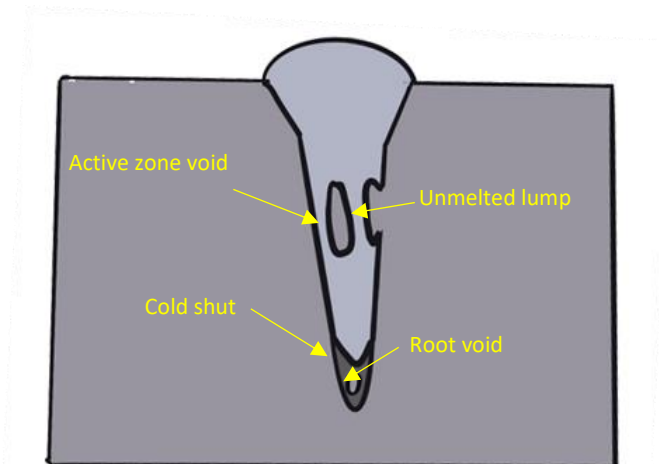

Figure 3: Schematic of EBW defects [17]

Various weld defects like porosity, un-melted lumps, spiking, and cold shut as seen in Fig. 3 were characterized and compared on EBW of eight different metals [18]. The root voids observed towards the tip of the penetration due to the entrapment of gases depended on the chemical composition of each material. The presence of gaseous elements like nitrogen and oxygen, and high vapor pressure elements like magnesium influenced the formation of these voids. Active zone voids formed in the vicinity of the beam travel path again depended on the presence of gaseous elements in the material and were directly proportional to beam current, power, and density. Un-melted lumps were seen around the active zone porosity. Spiking or long chains of porosity on top of the weld was formed due to arcing in the electron gun and formation.

2.5 Joining of L-PBF Metals

Varestraint tests conducted on tungsten inert gas (TIG) welded joints of L-PBF IN718 indicated that the as-printed welds had similar crack susceptibility as that of the wrought IN718 samples [19]. Cracking was associated with the formation of large grain structures after exposure to high temperatures leading to grain boundaries having higher stress concentration which led to crack initiation. The brazed joint of 4mm thick IN718 plate indicated two distinct zones at the joint namely the Isothermally Solidified Zone with a hardness of 460HV and the Diffusion Affected Zone with a hardness of 490HV [20]. The base metal had a hardness of 475HV. The brazed joint had a shear strength equal to 77% of the base metal.

EBW of L-PBF AlSi10Mg alloy was characterized with defects at the overlap of weld pools and had minimal HAZ [21]. Higher welding speeds led to deeper weld penetration but also produced higher porosity in the welds. The use of lower speeds at high heat input was found to produce higher porosity in weld metal than what was present in the base metal. The welds also had a lower hardness (103HV) as compared to the base metal (111HV).

The published information is yet to be found for EBW of L-PBF IN718 despite a growing demand for such applications. Thus, this research studies the L-PBF IN718 samples welded by EBW and compares the joint properties with the ASTM F3044-14a standard for AM IN718.

3 EXPERIMENTS

Gas atomized IN718 powder with an average particle size of 50μm was used for producing L-PBF test samples. The chemical composition (weight %) of the powder was: 51.99Ni, 18.58Cr, 19.73Fe, 5.17Nb, 3.02Mo, 0.99Ti, 0.49Al, 0.024C, 0.14Co, 0.12Cu, 0.073Si, and 0.074Mg. The samples (100x12.7x13mm) were printed on a Renishaw AM400 system with 275W laser power, 0.786m/s scanning speed, 110μm hatching distance, 60μm layer height, and stripe scanning pattern.

To represent and simulate an ideal welded condition (i.e., full penetration, precisely machined joint faces and accurately aligned parts), through-thickness EBW beads were produced on the tensile samples to simulate the ideal joining of two separate parts. The as-printed samples were welded using EBW with each combination of three levels of beam current and welding speed giving nine different heat inputs in the range 180 - 295J/mm necessary for deep weld penetrations (Table 1). Two repeats were produced to test the repeatability of the results. The electron beam was focused on the surface of the samples with a constant voltage of 50kV and in a vacuum environment of <1μTorr. The samples were arranged as seen in Fig. 4 with spacers to thermally insulate adjacent samples. The Sciaky EBW system was programmed with a non-oscillating beam moving perpendicular to the L-PBF build direction.

All welded samples were stress-relieved at 970°C for 1hr to mitigate any residual stresses generated during the EBW process. Coupons for hardness test (20x12.7x2.5mm) and weld geometry analysis were separated from the welded samples using wire-type Electrical Discharge Machining (Wire EDM). These coupons were labelled using unique markings and moulded in epoxy using a Struers CitoPress-15 machine for subsequent microhardness testing and microstructural studies.
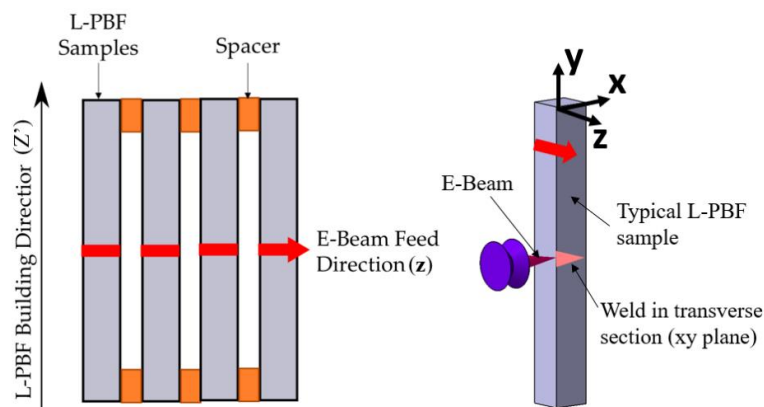

Figure 4: EBW process setup

Moulded samples were ground using Struers Abripol-20 grinding machine at five different grinding wheels - Emergy-80, Piano MD – 80, 220, 500, and 1200 grit in that sequence. Ground samples were cleaned ultrasonically in isopropyl alcohol for at least 2 minutes. The Dremel 3000 hand polisher and diamond pastes of 5-7µm, 1µm, and finally with 0.5µm abrasive size were used for polishing the samples. Aqua Regia etchant (4-part HCl (33%) + 1-part HNO3 (67%)) was swabbed on the polished coupons until the weld profile was visible. Wire EDM was used to machine the profile of tensile test samples as per ASTM E8 specification from the EBW samples. The top and bottom of the EBW samples were milled to achieve the required test sample thickness of 6mm. The milling process removed possible defective zones at the top and bottom of a weld. The schematic of the final tensile test samples is shown in Fig. 5.

The Olympus STM6 optical microscope was used to analyse the weld geometry and identify surface defects. High-resolution images of the welds and vicinities were enhanced using computer software to measure the weld penetration depth and weld area. The Wilson VH1102 Vickers hardness tester was used with a 300gf load and 15sec dwell time for hardness testing. Multiple indentations were performed at two levels A and B as shown in Fig. 6. Indentations were also performed at the weld centre between these two levels. The MTS 800 universal tester was used for tensile testing (100kN loadcell, 0.5mm/min pulling rate, and 5 Hz data acquisition frequency). The resulting stress-strain curves were analysed using computational methods to calculate yield strength, ultimate strength, fracture elongation, and toughness. Toughness was calculated based on the area under the stress-strain curve.

Table 1: EBW parameters

Sample	Welding Speed (mm/min)	Beam Current (mA)	Heat input (J/mm)
11A, 11B		65	295.3
12A, 12B	660.4	60	272.6
13A, 13B		55	249.8
14A, 14B		65	247.6
15A, 15B	787.4	60	228.6
16A, 16B		55	209.6
17A, 17B		65	213.2
18A, 18B	914.4	60	196.8
19A, 19B		55	180.4
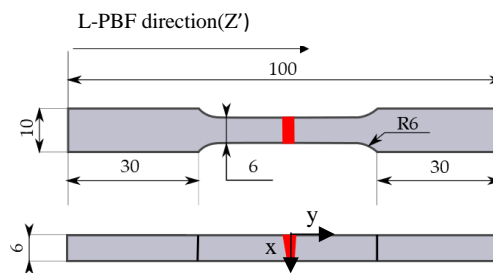
Figure 5: Front and top views of the tensile test sample fabricated as per ASTM E8 standard
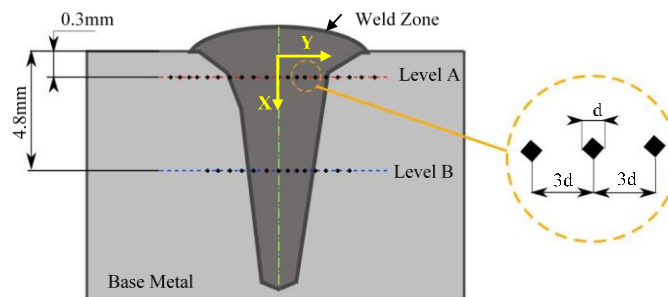
**Figure 6:** Microhardness testing across a typical weld

4 RESULTS AND DISCUSSION

4.1 Weld Geometry

Electron beam penetrated deep in all specimens and provided excellent weld penetration depths as seen in Fig. 7. The weld cross-section had a typical nail-shape: the top of the weld had a wide 'nail-head' shape which gradually reduced in width to a 'nail-tip' shape at the bottom. Longer exposure of the beam, larger effective diameter of the electron beam, and low thermal gradients led to a larger melt pool at the top, therefore, its larger width. Such nail-shape was consistent within all the welded samples.

Similar published results were found for electron beam welding of rolled IN718 [10], [12], [15]. The L-PBF base metal revealed the presence of defects such as gas-filled spherical pores, and irregularly shaped voids on their surface concentrated on the boundaries of the printed samples. These defects included: partially melted powder particles, shrinkage cavity of the molten pool on scanning surface, denudation of adjacent un-melted particles by the molten metal, scattered spatters along a scanning path, entrapment of environmental gas bubbles within the molten pool, etc. Similar defects were also reported for L-PBF metals [22]. When welding at heat inputs larger than 247.6J/mm, root voids were observed (Fig. 8) at the bottom of the weld in sample 13A (249.8J/mm). The high energy electron beam led to the violent melting and turbulent flow of the molten metal along its path and formed a crater with molten metal flowing upwards around the beam boundary. As the beam moved forward, the molten metal collapsed and solidified with a void at the weld-bottom that could not be filled owing to the fast cooling of the narrow strip of molten metal. Voids and spherical pores were also observed at the top of the weld on the interface of the weld zone and the base metal in some L-PBF samples as shown with sample 12A (272.6J/mm) in Fig. 8, and sample 17A (213.2J/mm) in Fig. 7. Due to the violent melting of metal powder during EBW process, the inert gas trapped in the pores or the voids of the base metal was released in the molten metal. Due to the heat of the molten metal, the released gas expanded or coalesced to form larger bubbles in the molten metal pool. The hot and low viscosity of molten metal inside the weld allows liquid metal to fill any shrinkage cavity and void; however, liquid metal with low viscosity of at the cooler junctions with parent material cannot fill the cavities, therefore, forming voids near the heat affected zones. These defects were not observed on the replicate of the sample, thereby, indicating their origin during the L-PBF process and not particularly during the EBW process.

A linear dependency of the weld penetration depth on the heat input is observed in Fig. 9. The overall weld area also increases with increasing electron beam current and decreasing of welding speed as seen in Fig. 10. As the beam voltage was constant at 50kV, the weld area also increased with an increase in the heat input. A slower beam speed, higher beam current, and eventually the higher heat inputs allowed longer interaction time between the beam and the material, forming a larger molten volume, deeper weld penetration, and weld area. Similar trends were concluded for EBW of rolled IN718 materials in other published articles [13], [15], [23], [24]. However, an opposite trend was reported for EBW of AlSi10Mg. The authors in this study concluded that a higher welding speed (lower heat input per equation (1)) would result in deeper weld penetration [21].
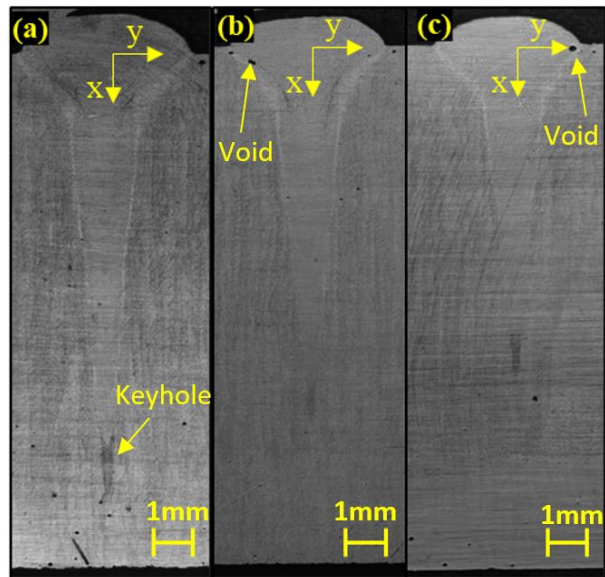
Figure 7: Typical nail-shape of weld profiles in samples (a) 11A (295J/mm), (b) 17A (213.2J/mm), and (c) 19A(180.4J/mm)
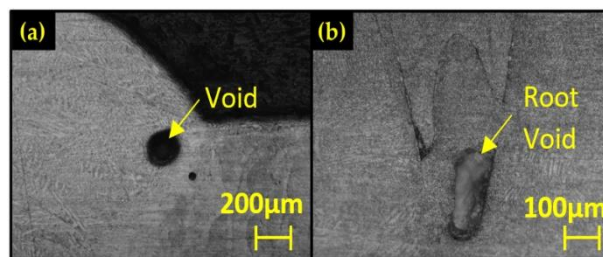
Figure 8: (a) Porosity in the nail head region at the top of the weld of sample 12A (272.6J/mm), (b) root void in the weld of sample 13A (249.8J/mm)
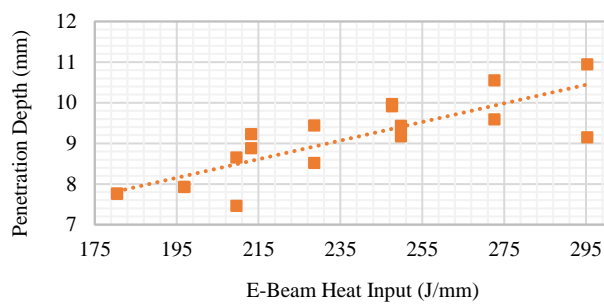
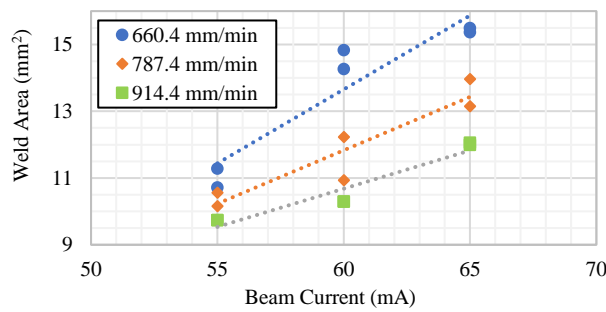**Figure 9:** Linear increase in penetration depth with heat input

Figure 10: Variation in weld area with beam current at various welding speeds

4.2 Microhardness

The typical microhardness result is shown in Fig. 11 where the origin of the coordinate system XY is located at the top of the weld zone as indicated in Fig. 6. The dotted lines in Fig. 11 indicate the weld zone width at the respective weld depth. The results show:

— The top of the weld was softer than the weld zone below for all samples. The nail-head zone, where the beam interacted with metal for a long time, contained larger grains, therefore, was softer than the material below it. A similar trend was observed for EBW of rolled IN718 samples [14].

— The weld zone was softer than the base metal. This was due to the rapid heating and cooling of the molten weld pool leading to a formation of inter-crystalline delta phases in the grain boundaries and having lesser strengthening phases and resulting in the reduction of the hardness in the fusion zone. The preferential grain structure in the rolled samples was disturbed due to the re-melting of the material during the welding process leading to the reduction in the hardness of these samples [14].

— Similar hardness trends were observed for samples welded at different heat inputs.
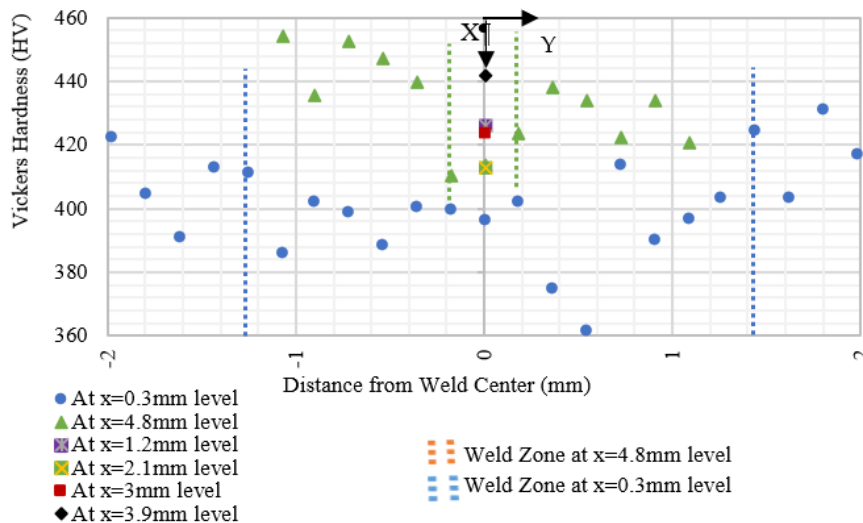

Figure 11: Microhardness test results of sample 19A/B (180.4J/mm)

4.3 Tensile Properties

The results of this research represent tensile properties for an ideal case when the full-penetration joint of two workpieces was precisely machined to make a tensile specimen without any misalignment. Fig. 12 represents a typical stress-strain curve for samples 19, 20, and their replicates. All tensile twin pairs have similar trends with reasonable repeatability. The tensile properties derived from the stress-strain curves of all samples are presented in Table 2. Figures 15-17 summarize the mechanical properties of all samples welded at different heat inputs, and compare them against the ASTM F3055-14a specifications for AM IN718.
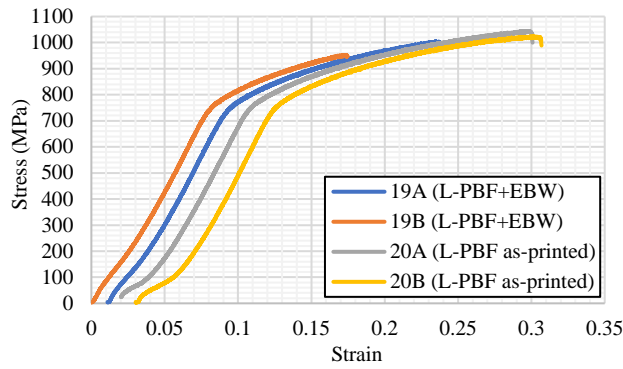
Figure 12: Typical stress-strain curves for EBW'ed samples 19A/B (180.4J/mm) and as-printed sample 20A/B. A slight horizontal shift (0.01 cumulative) of the data for samples 19A, 20A, and 20B was intentionally performed to avoid overlapping of the curves
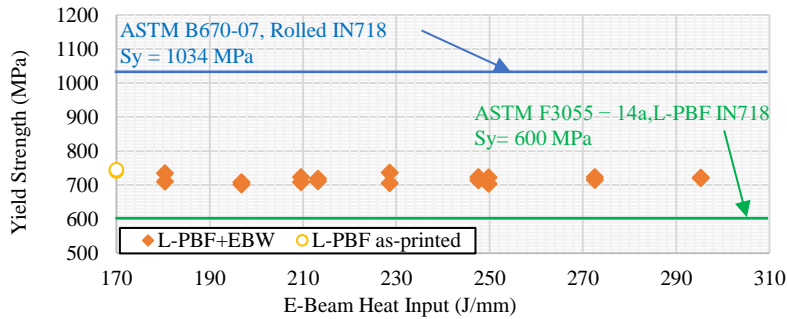
Figure 13: Effect of heat input on the yield strength of the EBW'ed samples
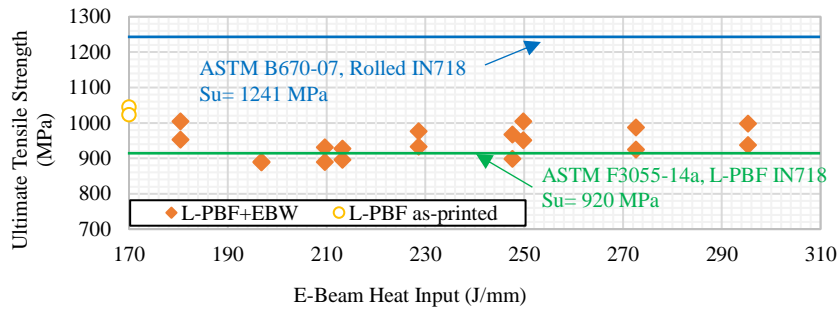
Figure 14: Effect of heat input on UTS of the EBW'ed samples
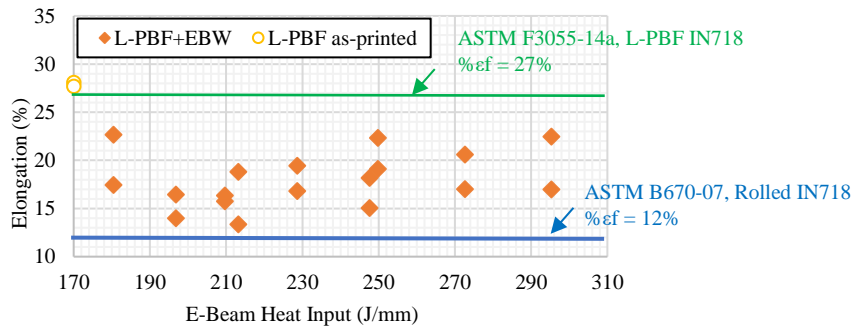
Figure 15: Effect of heat input on the elongation of the EBW'ed samples

The data from Figs. 13-15 suggest that:
— The measured yield strengths of all samples exceeded the ASTM specification for acceptable yield strength (600MPa) and the maximum yield strength of EBW of rolled IN718 from the previous study (571MPa)[15]
— For ultimate tensile strength, at least one replicate of each sample exceeded the ASTM specification of the acceptable tensile strength (920MPa) except for samples 18A/B (196.8 J/mm). The tensile strengths of L-PBF and EBW samples exceeded those of their rolled counterparts at each corresponding welding parameter [15].
— Although excellent yield and tensile strengths were obtained, the EBW samples were brittle and could not meet the ductility specification. However, the as-printed L-PBF samples 20A/B did meet the minimum ASTM specification (27%). Both sample types exceeded the ASTM B670-07 ductility requirements for rolled IN718. This was also verified by the higher toughness of the as-printed samples compared to the rest (Table 2). The EBW of rolled IN718 plates had better ductility (66% max elongation) as compared to the L-PBF counterparts due to the absence of inherent L-PBF defects [15].

4.4 Fractography

Fractured surfaces provided additional information that complements the tensile test results. Fig. 16 shows the coordinate system for the tensile specimen. All samples — except sample 16A (209.6J/mm) — were fractured at their respective weld zone (Figs. 17 (a)&(b)). This indicated the brittle nature of the L-PBF samples and their welds. The as-printed sample 20A fractured at a location within the gage length. Although the averaged ductility was high (28.1% in Table 2), the fractured surface revealed defects induced by the L-PBF process.
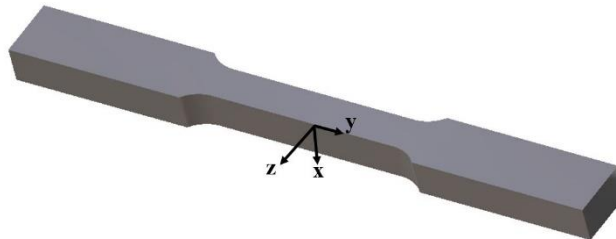

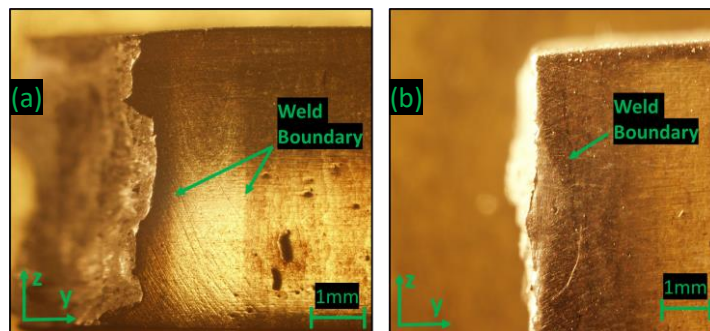**Figure 16:** Co-ordinate system for tested samples

Figure 17: (a) Sample 16A (209.6 J/mm) with the fractured surface outside of its weld zone; (b) Sample 18B (196.8 J/mm) with the fractured surface inside of its weld

Referring to Fig. 18, some un-melted IN718 powder particles were observed indicating a need for further optimization of the L-PBF parameters. These un-melted particles acted as weak spots and stress raisers in the material matrix and degraded the mechanical properties. Large fractured Laves phases were also seen in a ductile matrix.

The sample 16A (209.6J/mm) fractured outside the weld with low ductility (15.8% in Table 2) due to the presence of multiple defects: porosity on the surface of the sample which could have been inherited from the L-PBF process (Fig. 19a), and large brittlely fractured phases (Fig. 19 b). Those brittle phases were identified as NbC from the EDS analysis (Figs. 20a, b).

Table 2: Mechanical properties of EBW'ed samples

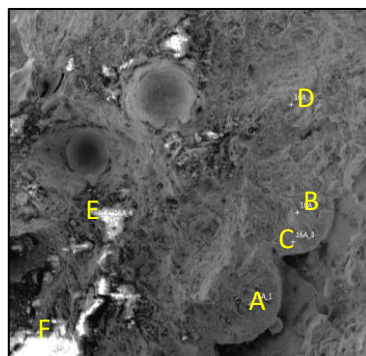| Sample Label	Heat Input (J/mm)	YS (MPa)	UTS (MPa)	Young's Modulus (GPa)	Elongation (%)	Toughness (J/mm³x 10⁻³)
11A/B	295.3	720, 722	937, 998	10.9, 10.5	16.9, 22.5	102, 155
12 A/B	272.6	715, 724	925, 987	11.0, 10.5	17.0, 20.6	98, 143
13 A/B	249.8	722, 703	951, 1004	10.8, 10.4	19.1, 22.3	117, 161
14 A/B	247.6	714, 724	899, 967	10.9, 10.7	15.1, 18.2	85, 102
15 A/B	228.6	737, 706	976, 932	10.9, 10.6	19.5, 16.8	125, 103
16 A/B	209.6	724, 709	889, 931	10.7, 11.6	15.8, 16.4	87, 102
17 A/B	213.2	719, 712	927, 899	10.9, 10.8	18.8, 13.4	125, 75
18 A/B	196.8	702, 708	891, 888	10.7, 11.2	16.5, 14	88, 77
19 A/B	180.4	735, 710	1004, 953	10.9, 11.1	22.7, 17.5	159, 110
20 A/B	----	741, 745	1045, 1024	10.8, 10.9	28.1, 27.7	210, 198
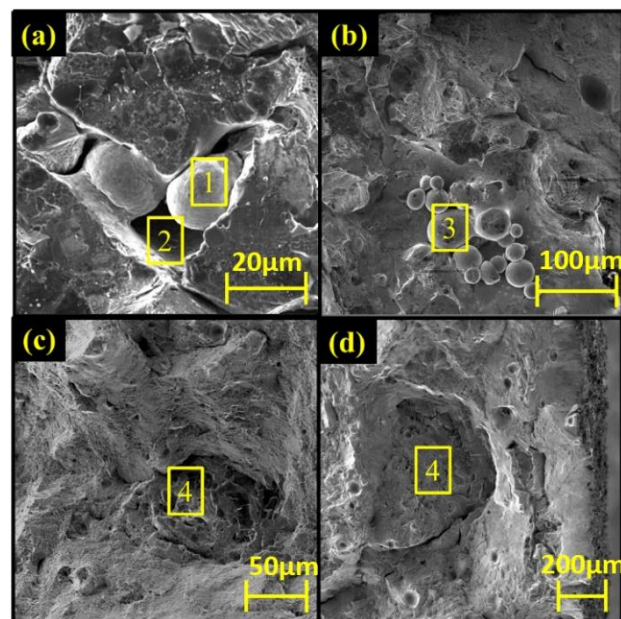
Figure 18: SEM fractography of sample 20A (as-printed L-PBF); (a, b): Un-melted powder particles (Label 1 & 3), unfilled zone (label 2); (c) & (d) brittle Laves zones (label 4)
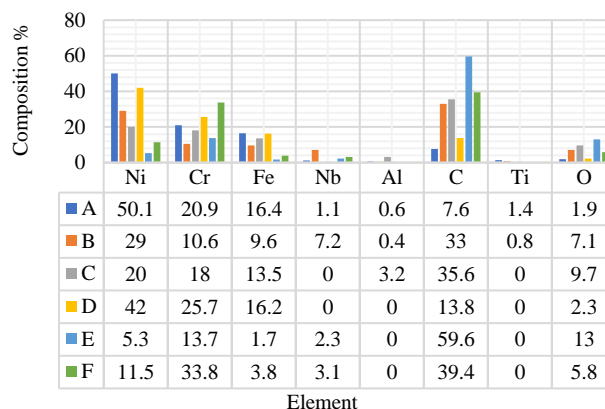
Fig. 21 (a) shows a smooth and flat surface indicating a disjointed L-PBF layer formed due to inadequate adhesion between adjacent layers on the EBW sample 17B (213.2J/mm). Subsequent EDS analysis confirmed the same elements and compositions of this layer and the surrounding matrix. Few spherical particles surrounded by a more ductile surface were also observed on the fractured surface of sample 17B (Fig. 21b). As this spherical particle was not melted and did not have any bond with the surrounding matrix, it was suspected that it could not be an IN718 powder but a possible contaminated powder or being a different material. An EDS analysis indicated the presence of a large percentage of aluminium (35.6-37.7%) and oxygen (49-51.4%) followed by titanium (7.3-9.6%) at certain sites (Fig. 22) as compared to the surrounding matrix (0% oxygen, 0.6% aluminium, and 1% titanium).
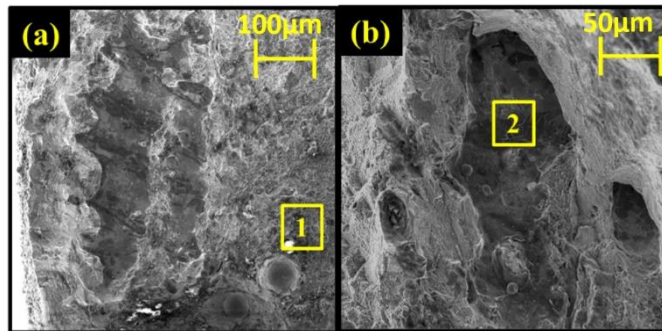
Figure 19: SEM fractography of EBW'ed sample 16A (209.6 J/mm) that fractured in the base metal; (a) Spherical pores (label 1) and (b) Brittle carbide phases (label 2)

(a)

(b)

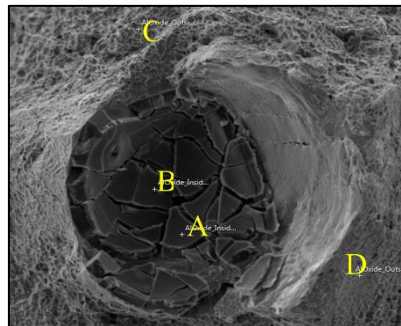|	Ni	Cr	Fe	Nb	Al	C	Ti	O
A	50.1	20.9	16.4	1.1	0.6	7.6	1.4	1.9
B	29	10.6	9.6	7.2	0.4	33	0.8	7.1
C	20	18	13.5	0	3.2	35.6	0	9.7
D	42	25.7	16.2	0	0	13.8	0	2.3
E	5.3	13.7	1.7	2.3	0	59.6	0	13
F	11.5	33.8	3.8	3.1	0	39.4	0	5.8

Element

Figure 20: (a) Fractured surface of sample 16A (209.6 J/mm), and (b) EDS analysis at different locations showing high carbon content

A study concluded that such phases were the brittle aluminium oxides Al_2O3 [25]. However, the resulted aluminium composition in the EDS analysis of 35.6-37.7 wt% Al was lower than the stoichiometric composition of Al_2O3 (52.925 wt% Al + 47.075 wt% O), it was postulated that the contaminant could be Al-Ti oxide instead. Better control of the L-PBF environment was recommended to prevent the formation of such oxides that adversely affect the mechanical properties of the L-PBF products.
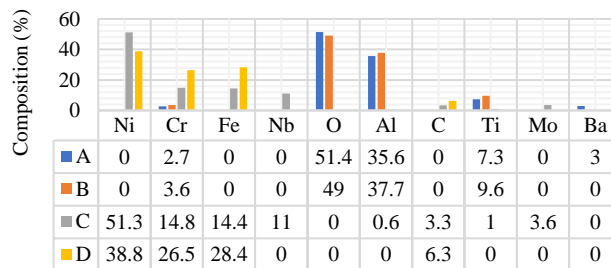
Both the L-PBF and EBW processes melted and solidified the workpiece metal, thereby, affected the microstructure of the base metal alloy. The rapid melting and cooling and later reheating of IN718 promoted the precipitation of solute metallic/ceramic compounds of niobium, carbon, titanium, aluminium with oxygen in the inter-dendritic region. This segregation led to the formation of hard and brittle carbides (such as NbC). All or most percentages of carbon in the alloy were consumed in this process. The higher the percentage of carbon in the base alloy matrix, the higher was the tendency of the carbide formation. This explained the presence of brittle carbides on the fractured surfaces of the L-PBF base metal and welded materials as seen in Figs. 18-19.
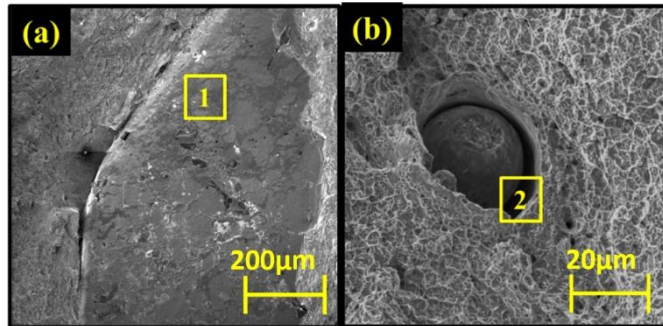
Figure 21: (a) Unfused L-PBF layer (label 1) and (b) Delaminated layer between the spherical contaminant and the material matrix (label 2) on the fractured surface of sample 17B (213.2 J/mm). This sample fractured in the weld zone

(a)

	Ni	Cr	Fe	Nb	O	Al	C	Ti	Mo	Ba
A	0	2.7	0	0	51.4	35.6	0	7.3	0	3
B	0	3.6	0	0	49	37.7	0	9.6	0	0
C	51.3	14.8	14.4	11	0	0.6	3.3	1	3.6	0
D	38.8	26.5	28.4	0	0	0	6.3	0	0	0

Elements

(b)

Figure 22: (a) Fracture of a brittle spherical particle in the ductile matrix of sample 17B (213.2 J/mm), and (b) EDS analysis at different locations showing high aluminium, titanium, and oxygen content

Further enrichment of the solute led to the formation of the Laves phase before the solidification process ended. The formation of such Laves phases was directly proportional to the presence of segregated niobium. Niobium segregation depended majorly on the cooling rate of the molten alloy. The higher the cooling rate, the lower was the segregation of niobium [7]. Thus, favourable material characteristics can be observed at high cooling rates during L-PBF or EBW. Niobium present in the alloy solution was shared by various secondary phases (δ, γ, γ', and γ'') during solidification. Thus, a higher percentage of any of these phases led to a reduction in the percentage of the others. In the case of the weld fusion zone, the percentage of strengthening phase γ' and γ'' reduced due to high consumption of Nb by the δ and γ phases[7], [14]. Further, the formation of Laves and δ phase in the grain boundaries provided favourable sites for the nucleation of voids and fissures.

Due non-uniform size of metal powder and coalescence of recycled powder particles, gaps were formed between the adjacent layers during the L-PBF process. This led to inadequate heat distribution and left some metal particles un-melted. The scanning laser beam induced thermal gradients between adjacent layers, thereby, fusing them and leading to a formation of homogenous metal in an ideal case. Uneven layer thickness, fluctuation of laser power, or powder contamination can form gaps between the adjacent layers (Fig. 21a). This led to inadequate heat distribution and partially melted powder particles in the materials as seen in Figs. 18a-b and 21b.

In summary, the brittleness of the L-PBF samples after electron beam welding was due to:
— Partially melted powder particles and unfused layers during the L-PBF process.
— Pores and voids due to trapped gas or solidification shrinkage.
— Carbide and oxide contaminants that fractured brittlely while preventing proper adhesion between adjacent layers.
— Delamination between the L-PBF layers.

The above defects were absent in wrought materials, therefore, the ductility of the EBW specimens of rolled IN718 is higher compared to that from L-PBF IN718. Eliminating defects with pre- or post-processes should improve the ductility of final products.

5 CONCLUSIONS

Electron beam joining of powder bed fused IN718 specimens was performed at different heat input levels. This study showed that:

1. Excellent penetration depth was achieved for EBW of L-PBF IN718 without beam oscillations. The penetration depth and weld area were directly proportional to the heat input.
2. Nail-shaped fusion zones were seen for all welded samples. The fusion zone was found to be softer as compared to the base metal hardness due to the dissolving of the strengthening γ' and γ'' precipitates.
3. All samples welded between 180-295 J/mm heat input either met or exceeded the specified tensile and yield strength from ASTM F3055-14a, however, the ductility of all the welded samples was below the ASTM specification due to inherent defected generated by L-PBF and EBW processes.
4. Fracture analysis revealed the presence of pores, partially melted powders, delaminated layers, brittle Laves phase, and other intermetallic/ceramic compounds. These defects contributed to the brittle nature of the EBW'ed samples.
5. Thermal induced defects were seen in both EBW of wrought and L-PBF IN718; however, additional defects in the latter materials would further degrade the mechanical properties of the welded specimen.

6 FUTURE WORKS

Remedial steps have been implemented to improve the properties of the weldments.

1. Optimizing the L-PBF parameters to minimize defects.
2. Improving the ductility of the welds by eliminating voids, Laves phase, and other brittle phases with post-processing heat treatment and hot isostatic pressing.

ACKNOWLEDGEMENT

REFERENCES

1. W. Bolen, "Certified Materials Test Report," West Virginia, 2019.
2. C. Slama and M. Abdellaoui, "Structural characterization of the aged Inconel 718," J. Alloys Compd., vol. 306, no. 1–2, pp. 277–284, 2000, doi: 10.1016/S0925-8388(00)00789-1.
3. J. Norrish, "High-energy density processes," in Advanced Welding Processes, J. Norrish, Ed. Elsevier, 2006, pp. 136–164.
4. G. Vander Voort, "Inconel 718 (Alloy 718) and Modified Inconel 718," 1991.
5. H. L. Eiselstein, "stp369-eb/apr. 1965 metallurgy of a columbium - hardened nickel - chromium - iron alloy," 2020.

6. G. A. Knorovsky, M. J. Cieslak, T. J. Headley, A. D. Romig, and W. F. Hammetter, "INCONEL 718: A solidification diagram," Metall. Trans. A, vol. 20, no. 10, pp. 2149–2158, 1989, doi: 10.1007/BF02650300.

7. G. D. Janaki Ram, A. Venugopal Reddy, K. Prasad Rao, and G. Madhusudhan Reddy, "Microstructure and mechanical properties of Inconel 718 electron beam welds," Mater. Sci. Technol., vol. 21, no. 10, pp. 1132–1138, 2005, doi: 10.1179/174328405X62260.

8. D. Deng, R. L. Peng, H. Brodin, and J. Moverare, "Microstructure and mechanical properties of Inconel 718 produced by selective laser melting: Sample orientation dependence and effects of post heat treatments," Mater. Sci. Eng. A, vol. 713, no. December 2017, pp. 294–306, 2018, doi: 10.1016/j.msea.2017.12.043.

9. J. Strößner, M. Terock, and U. Glatzel, "Mechanical and Microstructural Investigation of Nickel-Based Superalloy IN718 Manufactured by Selective Laser Melting (SLM)," Adv. Eng. Mater., vol. 17, no. 8, pp. 1099–1105, 2015, doi: 10.1002/adem.201500158.

10. C. A. Huang, T. H. Wang, C. H. Lee, and W. C. Han, "A study of the heat-affected zone (HAZ) of an Inconel 718 sheet welded with electron-beam welding (EBW)," Mater. Sci. Eng. A, vol. 398, no. 1–2, pp. 275–281, 2005, doi: 10.1016/j.msea.2005.03.029.

11. G. Madhusudhana Reddy, C. V. Srinivasa Murthy, K. Srinivasa Rao, and K. Prasad Rao, "Improvement of mechanical properties of Inconel 718 electron beam welds-influence of welding techniques and postweld heat treatment," Int. J. Adv. Manuf. Technol., vol. 43, no. 7-8, pp. 671–680, 2009,doi: 10.1007/s00170-008-1751-7.

12. M. Agilan, T. Venkateswaran, D. Sivakumar, and B. Pant, "Effect of Heat Input on Microstructure and Mechanical Properties of Inconel-718 EB Welds," Procedia Mater. Sci., vol. 5, pp. 656–662, 2014, doi: 10.1016/j.mspro.2014.07.312.

13. Y. Mei et al., "Effect of base metal and welding speed on fusion zone microstructure and HAZ hot-cracking of electron-beam welded Inconel 718," Mater. Des., vol. 89, pp. 964–977, 2016, doi: 10.1016/j.matdes.2015.10.082.

14. P. Gao, K. F. Zhang, B. G. Zhang, S. S. Jiang, and B. W. Zhang, "Microstructures and high temperature mechanical properties of electron beam welded Inconel 718 superalloy thick plate," Trans. Nonferrous Met. Soc. China (English Ed., vol. 21, no. SUPPL. 2, pp. s315–s322, 2011, doi: 10.1016/S1003-6326(11)61598-7.

15. V. Patel, A. Sali, J. Hyder, M. Corliss, D. Hyder, and W. Hung, "Electron Beam Welding of Inconel 718 Electron Beam Welding of Inconel 718," in Procedia Manufacturing, 2020, vol. 48, no. 2019, pp. 428–435, doi: 10.1016/j.promfg.2020.05.065.

16. J. Huang, "the Characterisation and Modelling of Porosity Formation in Electron Beam Welded Titanium Alloys," Computer (Long. Beach. Calif)., no. September, p. 207, 2011.

17. J. Kar, D. Chakrabarti, S. K. Roy, and G. G. Roy, "Beam oscillation, porosity formation and fatigue properties of electron beam welded Ti-6Al-4V alloy," J. Mater. Process. Technol., vol. 266, no. June 2018, pp. 165–172, 2019, doi: 10.1016/j.jmatprotec.2018.10.040.

18. Y. Arata, K. Terai, and S. Matsuda, "Characteristics of a Weld Defect and Its Prevention in Electron Beam Welding. Pt. 1. Characteristics of Weld Porosities," Trans. JWRI, no. Report I, 1973.

19. T. Raza, J. Andersson, and L. E. Svensson, "Varestraint weldability testing of additive manufactured alloy 718," Sci. Technol. Weld. Join., vol. 23, no. 7, pp. 606–611, 2018, doi: 10.1080/13621718.2018.1437338.

20. C. Xia, M. Zhao, W. Sun, H. Li, and P. Liu, "microstructure and properties of 3D printed Inconel 718 joint brazed with BNi-2 amorphous filler metal," Mater. Res., vol. 22, no. 1, pp. 1–10, 2018, doi: 10.1590/1980-5373-MR-2018-0348.

21. M. Nahmany, I. Rosenthal, I. Benishti, N. Frage, and A. Stern, "Electron beam welding of AlSi10Mg workpieces produced by selected laser melting additive manufacturing technology," Addit. Manuf., vol. 8, pp. 63–70, 2015, doi: 10.1016/j.addma.2015.08.002.

22. S. A. Khairallah, A. T. Anderson, A. Rubenchik, and W. E. King, "Laser powder-bed fusion additive manufacturing: Physics of complex melt flow and formation mechanisms of pores, spatter, and denudation zones," Acta Mater., vol. 108, pp. 36–45, Apr. 2016, doi: 10.1016/j.actamat.2016.02.014.

23. M. Thomas, P. Saha, G. Namboothiri, G. Radhakrishnan, and S. Srivastava, "Effect of process parameters on weld bead geometry and element segregation in Electron Beam Welding of INCONEL 718," pp. 717–722, 2017.

24. A. M. Saeed, M. Sobih, A. M. Youeesf, and A.-M. Ei-Batahgy, "Experimental Investigation of Laser and electron beam welding of Inconel 718," no. November 2015, 2016.

25. V. A. Popovich, E. V. Borisov, A. A. Popovich, V. S. Sufiiarov, D. V. Masaylo, and L. Alzina, "Impact of heat treatment on mechanical behaviour of Inconel 718 processed with tailored microstructure by selective laser melting," Mater. Des., vol. 131, no. January, pp. 12–22, 2017, doi: 10.1016/j.matdes.2017.05.065.